iScience

CellPress
OPEN ACCESS

Article

# Synergistic promotion of nitrogen vacancies and single atomic dopants on $Pt/C_3N_4$ for photocatalytic hydrogen evolution

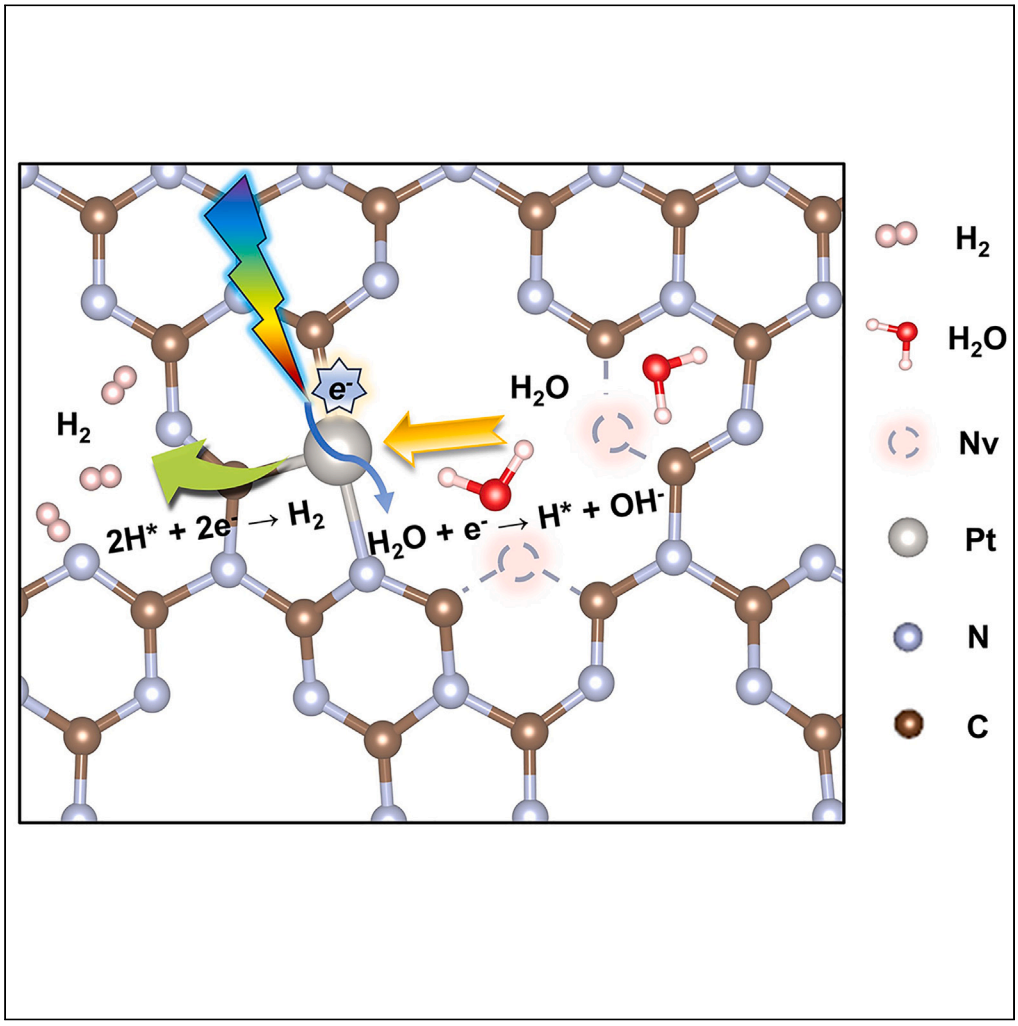


Ai-Ping Yan, Yu-Jue Qiu, Xing-En Wang, ..., Shun-Liu Deng, Jian-Wei Zheng, Su-Yuan Xie

sldeng@xmu.edu.cn (S.-L.D.)
jwzheng@xmu.edu.cn (J.-W.Z.)

## Highlights

Synergism between Pt atom and nitrogen vacancy is firstly inferred

A significantly high $H_2$ production rate of 3,890 μmol/g/h is achieved

New insight into the effect of Pt coordination environment on catalyst performances

Catalyst sustains high seawater $H_2$ yield, advancing sustainable solar $H_2$ extraction

Yan et al., iScience 27, 110420
August 16, 2024 
https://doi.org/10.1016/j.isci.2024.110420

iScience

CellPress
OPEN ACCESS

Article

# Synergistic promotion of nitrogen vacancies and single atomic dopants on Pt/$C_3N_4$ for photocatalytic hydrogen evolution

Ai-Ping Yan,[1,3] Yu-Jue Qiu,[1,3] Xing-En Wang,[1] Guang-Hua Wang,[2] Xian-Kui Wei,[1,2] Xin-Tian Li,[1] Xiao-Die Chen,[1] Xing Shang,[1] Shun-Liu Deng,[1,*] Jian-Wei Zheng,[1,4,*] and Su-Yuan Xie[1]

## SUMMARY

**$C_3N_4$ is widely applied in the synthesis of single-atom catalysts. However, understanding on the active site and the reaction mechanism is not fully in consensus. Especially, bare studies have considered the coordination environment of the single-atomic dopant and the effect of nitrogen vacancy on $C_3N_4$. In this study, we found that the presence of nitrogen vacancies promotes the activation of water and reduces the activation energy barrier for hydrogen generation. The results show that a synergistic effect between single-atom Pt and nitrogen vacancies enables the catalyst to achieve a superior hydrogen production rate of 3,890 μmol/g/h, which is 16.8 times higher than that of pristine $C_3N_4$. Moreover, the catalyst is also applicable for photocatalytic hydrogen production from seawater without significantly decreased hydrogen production rate. This study paves the way for the rational design and optimization of next-generation photocatalysts for sustainable energy applications, particularly in solar-driven hydrogen production.**

## INTRODUCTION

Graphitic carbon nitride ($C_3N_4$) is a typical type of advanced material with advantageously physical and chemical properties, such as notably high surface area, thermal stability, quantum efficiency, interfacial charge separation and transport, and ease of modification through either composite formation or the incorporation of desirable surface functionalities.[1,2] It is also an ideal support to prepare single-atom catalysts as $C_3N_4$ with abundant N atoms has favorable uncoordinated environment. Therefore, $C_3N_4$ has gained considerable attentions as an ideal candidate in the field of photo-, electro-, and thermal catalysis, especially in the field of solar fuels production through water splitting and $CO_2$ reduction, and environmental remediation through the degradation of organic pollutants.

As a promising material in heterogeneous catalysis, the role of $C_3N_4$ is generally clarified as a semiconductor or a support. Great efforts have been normally devoted into various strategies to enhance its role including morphological control,[3,4] heteroelement doping,[5–7] heterojunction construction,[8–11] and defect engineering.[12,13] In fact, the photoexcitons are the vital driving force of various chemical reactions in photocatalytic process; thereby their generation ability under photoirradiation determines the photocatalytic activity of semiconductor photocatalytic materials, directly affecting the final catalytic activities.[14] Apparently, introducing the single active sites with low potential into semiconductor photocatalytic materials can effectively promote the separation and migration of photoexcitons; thus higher photoactivity can be achieved due to highly inhibited recombination kinetics of photoexcitons.[15] Specifically, the $C_3N_4$ framework containing electron-rich N atoms can provide sufficient coordination sites and favorable space for capturing single-atom Pt through Pt-N bonding, making it a widely used support material for single-atom catalysts.[16,17] However, these approaches struggle to fundamentally improve charge separation and transfer efficiency because charges in short-range organic semiconductor lattices tend to be confined within planar space.[18–20] Besides modifying the band structure, most of these strategies are aimed at increasing the amounts of active sites by expanding the surface area and creating edge and nitrogen vacancies to coordinate more transition metal atoms.[21–24] These defects are thought to be filled by heteroatoms. Many single-atomic transition metals including Ru,[25] Pt,[26] Fe,[27] Cu,[28] Co,[29] and Ni[30] elements have been successfully anchored on $C_3N_4$. In additional to achieving 100% metal atom utilization, the single atoms act as electron acceptors to improve charge transfer, as well as active sites to activate reaction subtracts and intermediates.[31–33] It has also been proven that heteroatoms filled in the nitrogen vacancies of $C_3N_4$ show higher catalytic performances than those located on the plane or in the hole of $C_3N_4$.[34–36] Generally, it is recognized that these nitrogen vacancies create more opportunities for single atom to fill in so that the catalytic performance of reactions, for example photocatalytic water splitting, can be promoted.[16,17] However, scant attention has been paid to the effect of these nitrogen vacancies, which may not only create a position for the loading of single metallic atoms but also have a synergistic effect with the single atom in the activation of reaction

[1]State Key Laboratory of Physical Chemistry of Solid Surfaces, College of Chemistry and Chemical Engineering, Xiamen University, Xiamen 361005, China
[2]Innovation Laboratory for Sciences and Technologies of Energy Materials of Fujian Province (IKKEM), Xiamen 361005, China
[3]These authors contributed equally
[4]Lead contact
*Correspondence: sldeng@xmu.edu.cn (S.-L.D.), jwzheng@xmu.edu.cn (J.-W.Z.)
https://doi.org/10.1016/j.isci.2024.110420

intermediates. Notably, the coordination environment significantly changes when both the Pt atom and nitrogen vacancy coexist. Therefore, the electronic status and the reactivity should be strongly affected, resulting in the modification of their catalytic ability.

Herein, we firstly employed the first-principle density functional theory (DFT) to study the effect of nitrogen vacancies for water splitting over Pt single atoms loaded on $C_3N_4$. The coexistence of nitrogen vacancies and Pt single atom in an adjacent area is found to further promote the single-atomic catalysis in water splitting by activating water and enhancing the catalytic reactivity of Pt. Illuminated by the results of calculations, Pt single atoms on exfoliated $C_3N_4$ with different amount of nitrogen vacancies were deliberately prepared. Photocatalytic $H_2$ evolution from water is chosen as a probed reaction as $C_3N_4$ is typically and widely applied in the reaction. A series of characterizations including scanning electron microscopy (SEM), X-ray diffraction (XRD), synchrotron X-ray absorption spectroscopy (XAS), and aberration-corrected transmission electron microscopy (TEM) were employed to study the geometric structure of $C_3N_4$ and the dispersion of Pt species. Electron paramagnetic resonance (EPR) spectroscopy, X-ray photoelectron spectroscopy (XPS), UV-visible (UV-vis) diffuse reflectance spectroscopy, and valence band (VB) X-ray photoelectron spectroscopy (VB-XPS) were conducted to investigate the existence and states of nitrogen vacancies, as well as the effect of nitrogen vacancies on electronic structure of $Pt/C_3N_4$. Combining the characterization results, the synergistic effect is evident in the correlation between the amount of nitrogen vacancies and the hydrogen-generation performances. Finally, seawater is used as the substrate to extend the practical application. This work provides a new insight on the role of nitrogen vacancy for single-atomic doped $C_3N_4$, which shows a synergy with the single active site in the activation of reaction intermediates and the reactivity of active sites.

## RESULTS AND DISCUSSION

### Theory calculation

First-principle DFT was firstly employed to study the effect of nitrogen vacancies in $C_3N_4$ on the catalyst electronic structure and the water-splitting performance. Five models including $C_3N_4$, $C_3N_4$ with nitrogen vacancies ($C_3N_4$(Nv)), Pt single atoms doped in $C_3N_4$ ($Pt/C_3N_4$), Pt single atoms doped in the nitrogen vacancies of $C_3N_4$(Nv) ($Pt_{Nv}/C_3N_4$), and Pt single atoms doped in the nitrogen vacancies of $C_3N_4$(Nv) with one/two neighboring nitrogen vacancy/vacancies (christened as $Pt_{Nv}/C_3N_4$(Nv), $Pt_{Nv}/C_3N_4$(Nv2)) have been built (Figures 1A–1C). The adsorption energy of Pt single atoms in $Pt_{Nv}/C_3N_4$ and $Pt_{Nv}/C_3N_4$(Nv) is significantly higher than that in $Pt/C_3N_4$ (−8.74 eV and −8.57 eV versus −3.07 eV as listed in Table S1), indicating that the presence of nitrogen vacancies is beneficial for the deposition of Pt single atoms.

Density of states (DOS) and band structures for $C_3N_4$, $C_3N_4$(Nv) and $Pt/C_3N_4$(Nv) are investigated to study the electronic structure of these models. As shown in Figures 1D–1F and S1, upon introducing a nitrogen vacancy into $C_3N_4$, the band-gap energy of $C_3N_4$(Nv) decreases from 2.75 eV to 2.64 eV. Moreover, a defect level formed by C2p and N2p orbitals emerges within the band gap (Figure S1C). Both C2p and N2p orbitals contribute to the conduction band (CB) of $C_3N_4$, while the VB is predominantly composed of N2p orbitals, in agreement with previously reported findings.[37] Upon incorporating Pt single atom into $C_3N_4$, the band-gap energy of $Pt/C_3N_4$ further decreases from 2.75 eV to 2.05 eV, accompanied by appearance of an impurity level within the band gap. In the case where Pt is introduced into the location of the nitrogen vacancy in $C_3N_4$(Nv), the band-gap energy drops from 2.64 eV to 2.53 eV, and no distinct defect or impurity level is observed. Further introduction of a nitrogen vacancy next to the Pt single atom in $Pt_{Nv}/C_3N_4$(Nv) leads to a further reduction in the band-gap energy from 2.53 eV down to 2.25 eV. These results confirm that the coexistence of Pt single atom and nitrogen vacancies contributes to the narrower band gap in $Pt_{Nv}/C_3N_4$(Nv) compared to pristine $C_3N_4$. Analogously, DOS indicates coexistence of Pt single atom and nitrogen vacancies in $Pt_{Nv}/C_3N_4$(Nv) (as shown in Figures 1G and S1) shifts the d−band center from −0.87 eV to −4.18 eV compared with $Pt/C_3N_4$, elucidating that the electronic structure has a strong correlation with the coordination environment of Pt single atom, which can thus affect their catalytic performances.

Hydrogen evolution typically consists of two fundamental steps: the initial Volmer reaction (Equation 1) followed by either the Heyrovsky reaction (Equation 2) or the Tafel reaction (Equation 3)[38] as shown in the following:

$$H_2O + e^- \rightarrow H^* + OH^- \quad \text{(Equation 1)}$$

$$H^* + H_2O \rightarrow H_2 + OH^- \quad \text{(Equation 2)}$$

$$2H^* \rightarrow H_2 \quad \text{(Equation 3)}$$

Therefore, the activation of water may have a significant effect on the Volmer step and the Heyrovsky step. As shown in Figures 1H and S2, the adsorption energies of water on pristine $C_3N_4$ and $C_3N_4$(Nv) are −0.40, and −0.41 eV, respectively, which are regarded as relatively weak physical adsorption. After loading Pt single atom onto $C_3N_4$(Nv), the adsorption energy of water molecules slightly decreases to −0.35 eV on $Pt/C_3N_4$. However, the adsorption energy significantly increases to −0.96 eV when Pt substitutes a nitrogen vacancy on $Pt_{Nv}/C_3N_4$. Furthermore, the nitrogen-vacancy-substituted Pt single atom has a synergistic effect with the proximal nitrogen vacancies when there is one or two nitrogen vacancy (vacancies) near the Pt single atom on $Pt_{Nv}/C_3N_4$(Nv) and $Pt_{Nv}/C_3N_4$(Nv2). The adsorption energy dramatically increases to −1.50 eV and −1.49 eV, respectively. These results indicate that the introduction of nitrogen vacancies on the single Pt atom-doped $C_3N_4$(Nv) catalyst can promote the activation of water with a reduced steric hindrance in the Volmer step and the Heyrovsky step. As a consequence, the

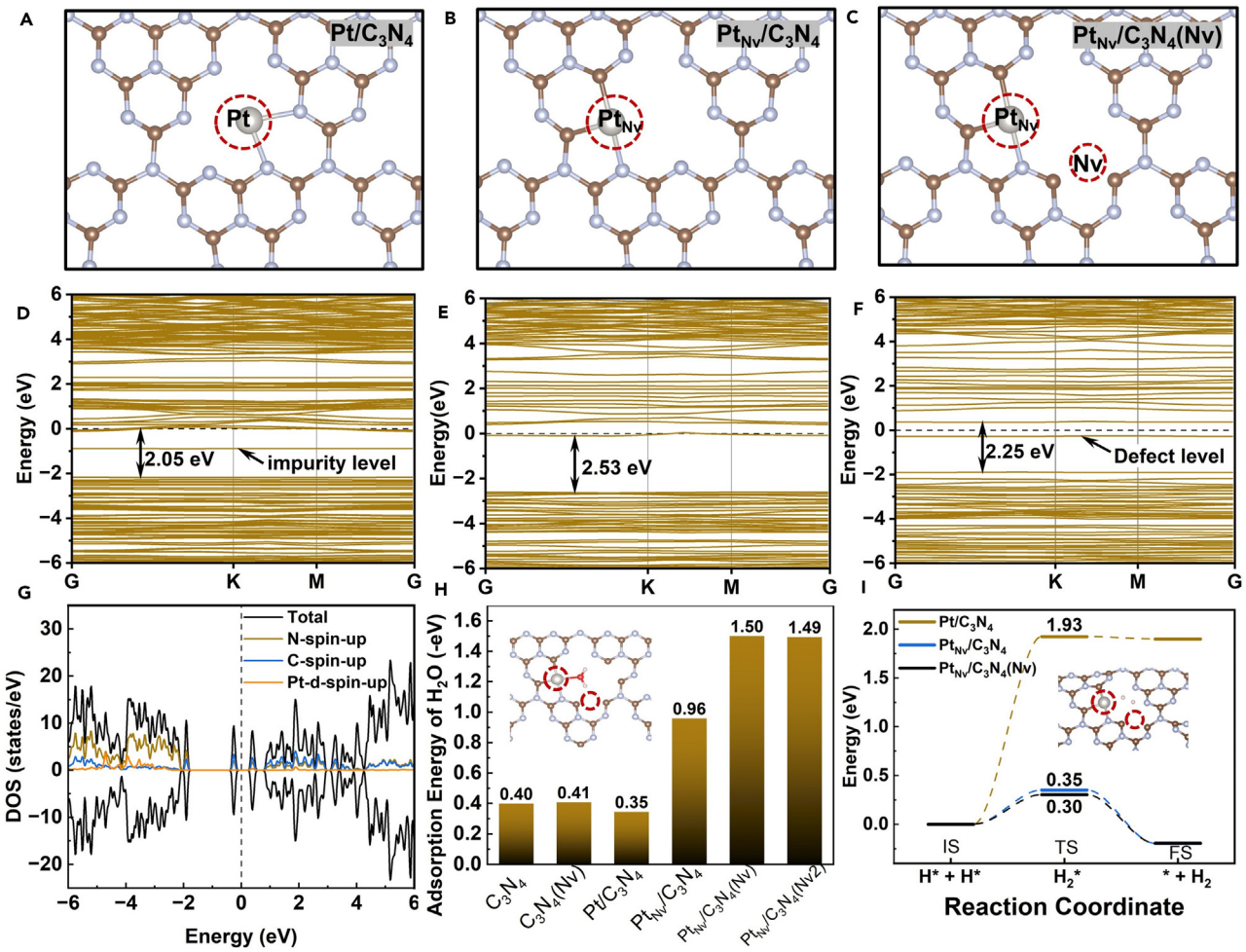


**Figure 1. Structure models and corresponding calculated band structures**

(A and D) Pt/$C_3N_4$, (B and E) $Pt_{Nv}/C_3N_4$, and (C and F) $Pt_{Nv}/C_3N_4$(Nv); (G) density of states (DOS) of $Pt_{Nv}/C_3N_4$(Nv); (H) adsorption energy of $H_2O$ on $C_3N_4$, $C_3N_4$(Nv), Pt/$C_3N_4$, $Pt_{Nv}/C_3N_4$, $Pt_{Nv}/C_3N_4$(Nv), and $Pt_{Nv}/C_3N_4$(Nv2). Inset is a model of a water molecule adsorbed on $Pt_{Nv}/C_3N_4$(Nv); (I) free-energy diagram of hydrogen evolution over the Pt/$C_3N_4$, $Pt_{Nv}/C_3N_4$ and $Pt_{Nv}/C_3N_4$(Nv). Inset is the model of the transition state (TS) of a $H_2$ molecule adsorbed on the $Pt_{Nv}/C_3N_4$(Nv). IS and FS represent initial state and final state. The single Pt atom and nitrogen vacancy are included in red circles.

activation energy for the $H_2$ generation from hydrogen atom was modified over Pt/$C_3N_4$, $Pt_{Nv}/C_3N_4$, and $Pt_{Nv}/C_3N_4$(Nv). As shown in Figure 1I, the activation energy barrier for the combination of hydrogen atoms into $H_2$ in the Tafel step is 1.93 eV for Pt/$C_3N_4$. The activation energy over $Pt_{Nv}/C_3N_4$ significantly decreases to 0.35 eV. This confirms that the introduction of nitrogen vacancy for the substitution of Pt single atom can dramatically improve the generation of $H_2$. Notably, the activation energy barrier for $H_2$ evolution further decreases to 0.30 eV over $Pt_{Nv}/C_3N_4$(Nv), confirming that a synergy should exist between Pt single atom and nitrogen vacancy, leading to the promotion of $H_2$ evolution from water.

## Catalyst synthesis and structural analysis

The synthesis procedure of $C_3N_4$(Nv) and $Pt_{Nv}/C_3N_4$(Nv) is illustrated in Figure 2A; $C_3N_4$ is firstly prepared by annealing urea at 550°C in air. Subsequently, the obtained $C_3N_4$ was pretreated in $N_2$ at 550°C, 600°C, and 650°C to afford $C_3N_4$(Nv) with different content of nitrogen vacancies. Finally, Pt atoms are deposited on $C_3N_4$ and $C_3N_4$(Nv) pretreated at different temperature by wet impregnation to obtain Pt/$C_3N_4$, $Pt_{Nv}/C_3N_4(Nv_{550})$, $Pt_{Nv}/C_3N_4(Nv_{600})$, and $Pt_{Nv}/C_3N_4(Nv_{650})$. To be noticed, DFT models are ideal while the actual sample should have mixed structures containing the DFT models. So, these samples do not have a direct corresponding relationship with the DFT models. However, they show a trend that, for the increment of the content of nitrogen vacancies, more single atom Pt can occupy the nitrogen sites ($Pt_{Nv}$). Also, further increasing the content of nitrogen vacancies, more nitrogen vacancies can be proximal to Pt single atom $Pt_{Nv}/C_3N_4$(Nv). Therefore, $Pt_{Nv}/C_3N_4(Nv_{550})$ has more local structures similar to $Pt_{Nv}/C_3N_4$ compared to other samples. $Pt_{Nv}/C_3N_4(Nv_{600})$ and $Pt_{Nv}/C_3N_4(Nv_{650})$ should have more local structures similar to $Pt_{Nv}/C_3N_4$(Nv) and $Pt_{Nv}/C_3N_4$(Nv2). This can be confirmed by the following structural analysis.

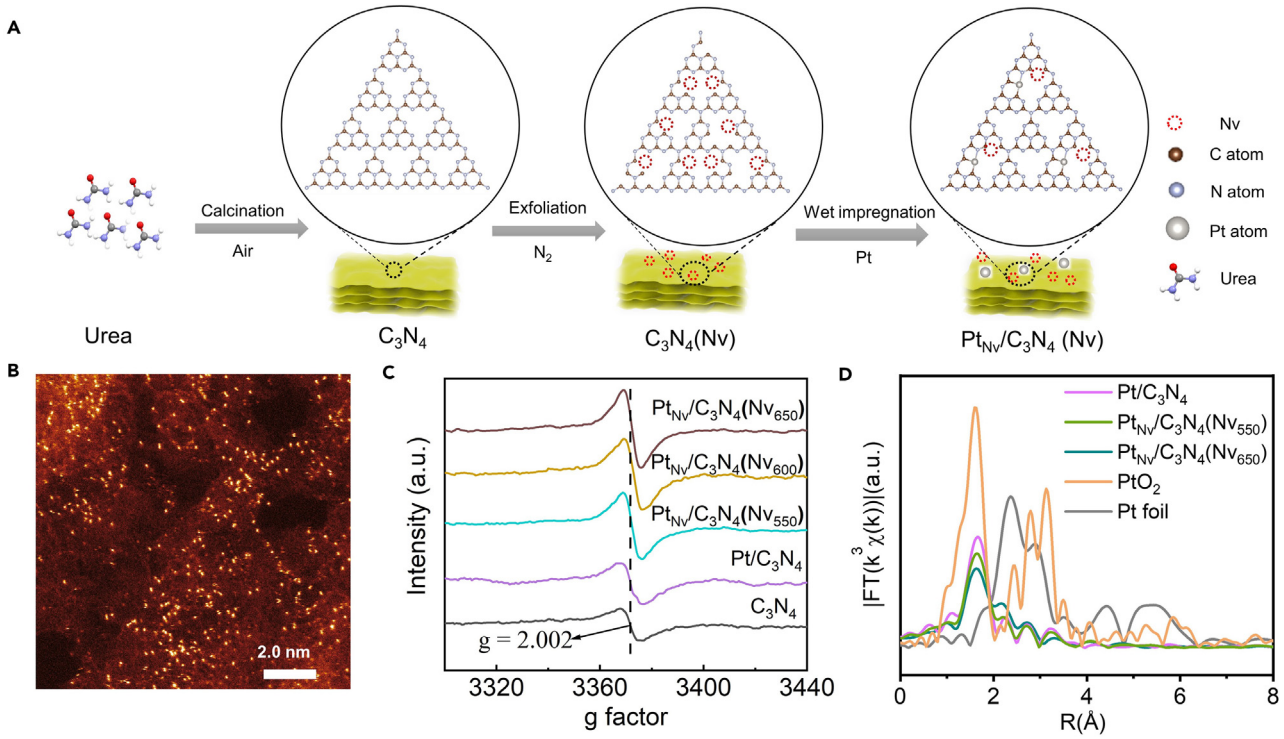


**Figure 2. Preparation and structural characterization**

(A) Scheme of the synthesis procedure of $C_3N_4$(Nv) and $Pt_{Nv}/C_3N_4$(Nv).

(B) STEM-HAADF images of $Pt_{Nv}/C_3N_4(Nv_{600})$.

(C and D) (C) EPR spectra and (D) corresponding $k^3$-weighted FT spectra at R space of Pt foil, $Pt/C_3N_4$, $Pt_{Nv}/C_3N_4(Nv_{550})$, and $Pt_{Nv}/C_3N_4(Nv_{650})$.

The morphology and microstructure of the samples were investigated by using a series of characterization techniques including nitrogen adsorption, microscopy, and XRD. XRD patterns (Figure S3) indicate that all the samples exhibit a strong diffraction peak near the high angle at $2\theta = 27.8°$ and a weaker one close to the low angle at $2\theta = 12.7°$. These peaks are attributed respectively to the interplanar stacking of aromatic C-N heterocycles (the (002) plane) and the intraplanar repetitive units of triazine rings (the (100) plane) as per JCPD card no. 87-1526.[39] The similarity in XRD patterns among the five samples suggests that the introduction of nitrogen vacancies and the loading of single-atomic Pt do not alter the crystal structure of $C_3N_4$. An atomic model for $C_3N_4$ constructed from melon (melon-like) units is also depicted in Figure S3.[40] Aluminum oxide is used as a reference to compare the intensities of XRD signals. After normalization, the peak intensity of the (002) plane decreases as the exfoliation temperature increases. This is due to the thermal delamination effect during high-temperature calcination, leading to larger layer spacing and lower XRD peak intensities. Consistent with the result of XRD patterns, SEM images in Figure S4 also exhibit a porous layered morphology without obvious changes after the introduction of nitrogen vacancies. The increase in specific surface area for $Pt_{Nv}/C_3N_4(Nv_{550})$ and $Pt_{Nv}/C_3N_4(Nv_{650})$ is not so significant, insinuating that the surface area is not a major factor improving the activity (Figure S5 and Table S2). Upon characterizing different regions using TEM (Figure S6), there are no discernible particles on the surface of $C_3N_4$ nanosheets, thus ruling out the existence of Pt nanoparticles. This observation aligns with the XRD results presented in Figure S3, where no diffraction peaks corresponding to metallic Pt nanoparticles are found in the XRD patterns. However, a Pt loading of around 1 wt % close to the theoretical value was measured for all the Pt-supported $C_3N_4$ and $C_3N_4$(Nv) (Table S3). These insinuate that Pt exists predominantly in the form of single atoms or highly dispersed species within the $C_3N_4$ matrix. Aberration-corrected high-angle annular dark-field scanning transmission electron microscopy (STEM-HAADF) measurement was then conducted. As illustrated in Figure 2B, a dense distribution of bright spots with diameters smaller than 0.2 nm is evident on the $C_3N_4$(Nv) substrate, confirming that Pt species exists as single atoms, consistent with the assumption from XRD and TEM.

To investigate the content of nitrogen vacancies, EPR spectroscopy characterization was carried out. As shown in Figure 2C, all samples including $C_3N_4$, Pt-supported $C_3N_4$, and $C_3N_4$(Nv) exhibit a Lorentzian line with a g value of 2.002 attributed to the presence of unpaired electrons in $sp^2$-hybridized carbon atoms within the $\pi$-conjugated aromatic rings.[41] Compared with pristine $C_3N_4$, stronger EPR signals are observed for Pt supported on $C_3N_4$ with higher exfoliation temperature in $N_2$, and $Pt_{Nv}/C_3N_4(Nv_{650})$ shows the strongest signal.[42] This enhancement indicates the successful creation of nitrogen vacancies which may facilitate the transfer for photogenerated charges. The Fourier transform infrared (FTIR) spectra display three types of characteristic vibrational absorption peaks: a sharp peak at around 810 $cm^{-1}$, a set of peaks within the range of 1,200–1,700 $cm^{-1}$, and a broad peak between 2,800 and 3,500 $cm^{-1}$ (Figure S7). These correspond to the bending vibration of triazine rings, the stretching vibrations of aromatic C-N heterocycles, and the stretching vibrations of -$NH_x$ (where x = 1,2) groups

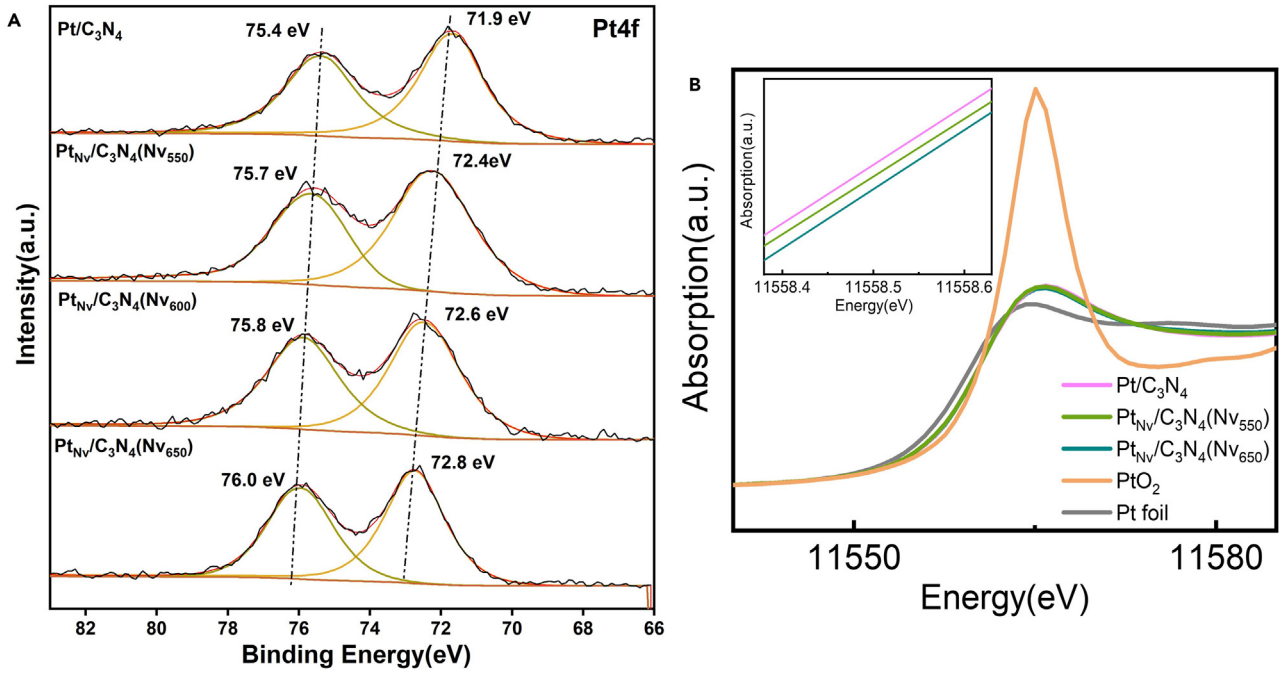


**Figure 3. XPS and XANES spectra**

(A) Pt 4f XPS spectra Pt/$C_3N_4$, $Pt_{Nv}/C_3N_4(Nv_{550})$, $Pt_{Nv}/C_3N_4(Nv_{600})$, and $Pt_{Nv}/C_3N_4(Nv_{650})$ and (B) XANES spectra of Pt foil, Pt/$C_3N_4$, $Pt_{Nv}/C_3N_4(Nv_{550})$, and $Pt_{Nv}/C_3N_4(Nv_{650})$. Inset image is the enlarged pre-edge of Pt/$C_3N_4$, $Pt_{Nv}/C_3N_4(Nv_{550})$, and $Pt_{Nv}/C_3N_4(Nv_{650})$.

located at the edges of the $C_3N_4$ framework, respectively.[43,44] Notably, after high-temperature treatment in $N_2$, the intensity of the peak at 810 $cm^{-1}$ tended to reduce in $Pt_{Nv}/C_3N_4(Nv)$ pretreated at higher temperature, which could be attributed to the disruption of C-N bonding sites in the triazine rings, indicating the successful introduction of nitrogen vacancies,[40] Although $Pt_{Nv}/C_3N_4(Nv_{600})$ does not decrease clearly. This may be due to the baseline interference from other species (for example, species at 730 $cm^{-1}$) or water.

Further exploration of the coordination environment of Pt in the catalysts was conducted using extended X-ray absorption fine structure (EXAFS) characterization. After Fourier transformation (FT) processing and weighting by $k^3$, the EXAFS spectra revealed a single peak in samples of Pt/$C_3N_4$, $Pt_{Nv}/C_3N_4$ ($Nv_{550}$), and $Pt_{Nv}/C_3N_4$ ($Nv_{650}$) (as shown in Figure 2D), corresponding to the first coordination shell of Pt, which can be attributed to Pt-C/N interactions.[45,46] In comparison, the standard Pt foil sample presents a strong peak at 2.36 Å, which is associated with Pt-Pt coordination. However, in the EXAFS spectra of single-atom Pt catalysts, such a peak is typically absent with a Pt-O feature instead, and no characteristic signal of Pt-Pt coordination is observed in the EXAFS spectra of Pt/$C_3N_4$, $Pt_{Nv}/C_3N_4(Nv_{550})$, and $Pt_{Nv}/C_3N_4(Nv_{650})$, indicating that Pt atoms are atomic dispersed without forming Pt-Pt bonds. In Pt/$C_3N_4$, $Pt_{Nv}/C_3N_4(Nv_{550})$, and $Pt_{Nv}/C_3N_4(Nv_{650})$, the coordination numbers of Pt–C/N are 5.1, 4.3, and 3.9, with average bond lengths of about 2.07, 2.07, and 2.09 Å, respectively (Table S5). This substantiates that the predominant vacancy type in the samples is N2C, given that N3C defects typically exhibit a coordination number of 3 and confirms the existence of nitrogen vacancies near Pt. The increased bond length coincides with the model of the coexistence of Pt single atom and nitrogen vacancy in proximal position.

XPS was employed to investigate the chemical status of Pt, C, and N species on the surface of various photocatalysts (Figures 3 and S8–S10). C 1s peak at 284.8 eV associated with amorphous carbon (C-C/C=C) within the $C_3N_4$ is used as the reference value to calibrate the binding energies across the entire spectra. The peak corresponding to N-C=N groups in the aromatic rings of the carbon nitride molecule moves toward lower binding energy from 288.3 eV to 288.1 eV with higher pretreated temperature when nitrogen vacancies are generated (Figures S9A and S10A). In the N1s spectra, three main peaks can be discerned. The peak at ~398.6 eV represents $sp^2$-hybridized N atoms in the C-N=C bonds of the triazine rings. The peak at ~399.7 eV attributes to bridging N atoms in the central positions of the heptazine rings, and the peak at 401.2 eV signifies N atoms in terminal amino groups -$NH_x$. These peaks show a trend of shifting toward higher binding energy (Figures S9B and S10B). And the decrease in the intensity of N2C (-$NH_x$) is compelling evidence for the formation of N2C vacancies on the surface of $C_3N_4$(Nv). In addition, the peaks of Pt 4f spectra at ~72 eV and 75.4 eV are ascribed to $Pt^{2+}$ and no characteristic peak appears for Pt metal (Figure 3A). This further indicates that Pt is atomic dispersion coordinated with C and/or N atoms. Interestingly, with the additional amount of nitrogen vacancies, Pt peaks shift toward higher binding energy. These shifts are because of the strong interaction between Pt single atom with 3d unoccupied orbitals and N with lone pair electrons in $C_3N_4$. The increased content of nitrogen vacancies causes less coordination amounts with Pt, as well as less electrons transfer from N species to Pt species, resulting in a higher oxidation state of Pt species, which thus may favor the reaction of photocatalytic $H_2$ evolution[47] with electron-deficient Pt active sites. Figure 3B presents the Pt X-ray absorption near-edge structure (XANES) spectra of samples Pt/$C_3N_4$, $Pt_{Nv}/C_3N_4(Nv_{550})$, and $Pt_{Nv}/C_3N_4(Nv_{650})$, showing that the absorption

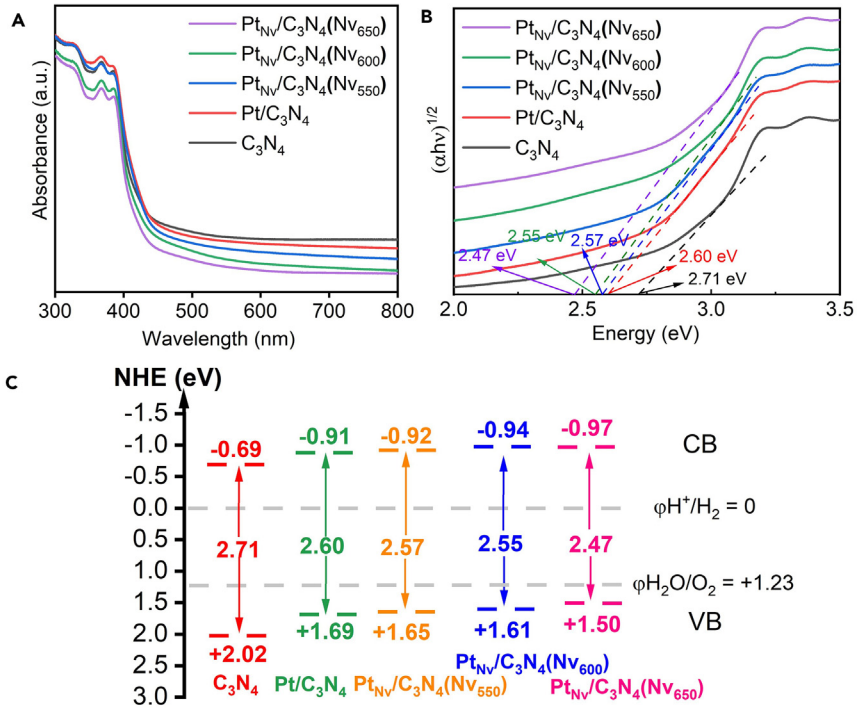


**Figure 4. Band structure**

(A) UV-vis absorption spectrum.

(B) The band gap obtained based on the Tauc formula.

(C) Band structure of $C_3N_4$, $Pt/C_3N_4$, $Pt_{Nv}/C_3N_4(Nv_{550})$, $Pt_{Nv}/C_3N_4(Nv_{600})$, and $Pt_{Nv}/C_3N_4(Nv_{650})$.

pre-edges of all samples are at higher energy than that of the standard Pt foil. And an energy redshift is observed for $Pt_{Nv}/C_3N_4(Nv)$ with higher pretreated temperature, arising from the electronic interaction between the single-atom Pt and the nitrogen vacancies. This electronic interaction between single-atom Pt and the nitrogen vacancies is enhanced with increasing nitrogen vacancy content, leading to more electron deficiency. The result is consistent with XPS results.

## Optical and photoelectrochemical properties

To study the electronic structure of the samples, UV-vis and VB-XPS were then carried out. Pt presented in the form of single atoms coordinated to nitrogen atoms. Therefore, the samples can be treated as pure sample to use the Kubelka-Munk formula. As shown in Figure 4A, the light-absorption band of $Pt_{Nv}/C_3N_4(Nv_{550})$, $Pt_{Nv}/C_3N_4(Nv_{600})$, and $Pt_{Nv}/C_3N_4(Nv_{650})$ in the range of 450 nm–800 nm has a red shift. The introduction of nitrogen vacancies and single-atom Pt causes a significantly enhanced absorption.[48] As shown in Figure S11, the color of the samples becomes deeper with an increased concentration of nitrogen vacancies. Therefore, the electronic structure should change with the introduction of nitrogen vacancies. The Kubelka-Munk method was then employed to transform UV-vis to obtain the corresponding Tauc plot. Pt presented in the form of single atoms coordinated to nitrogen atoms. Therefore, the samples can be treated as pure sample to use the Kubelka-Munk formula. As depicted in Figure 4B, the band-gap energies (Eg) of the five samples including $C_3N_4$, $Pt/C_3N_4$, $Pt_{Nv}/C_3N_4(Nv_{550})$, $Pt_{Nv}/C_3N_4(Nv_{600})$, and $Pt_{Nv}/C_3N_4(Nv_{650})$ are 2.71 eV, 2.60 eV, 2.57 eV, 2.55 eV, and 2.47 eV, respectively. The Eg is gradually decreased, which coincids with the result DOS, confirming that the introduction of single Pt dopants and nitrogen vacancies can lower the band gap to improve the reactivity. The CB positions of the synthesized materials can be determined based on the Tauc plot derived from the solid UV diffuse reflectance spectra, while the accurate VB positions of each sample can be obtained from the XPS VB spectra (VB-XPS), with the Fermi level as the reference (Figure S12). Consequently, the energy band structure of the catalysts could be afforded as illustrated in Figure 4C. $Pt_{Nv}/C_3N_4(Nv)$ possesses more negative reduction potentials, which is in favor of $H_2$ activation and may promote the $H_2$ evolution. The band gap is reduced following the trend of the nitrogen vacancy concentration increment, which coincides with the DFT calculation except for $Pt/C_3N_4$ and $Pt_{Nv}/C_3N_4(Nv)$. In the DFT band structure calculations, we neglected the influence of defect level or impurity level. If we account for the impact of defect level or impurity level, the estimated band gaps for $Pt/C_3N_4$ and $Pt_{Nv}/C_3N_4(Nv)$ would be revised to 0.767 eV and 0.637 eV, respectively. This adjustment aligns with the fact that nitrogen vacancies serve to reduce the band gap. The narrower band gap leads to stronger responsiveness to visible light and easier formation of free photogenerated charge carriers. Also, based on the DFT calculation results, the coexistence of single-atom Pt and nitrogen vacancy could enhance the water activation and reduce the energy barrier for $H_2$ generation. Ultimately, the photocatalytic hydrogen production performance could be improved.

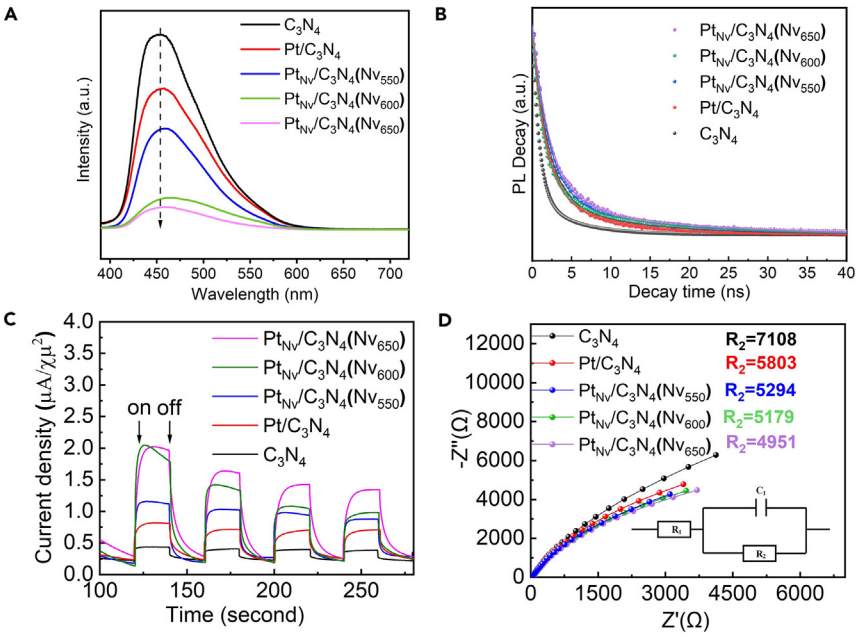


**Figure 5. Characterization of photogenerated electron migration behavior**

(A) Steady-state photoluminescence (PL) spectra.

(B) Time-resolved PL spectra.

(C) Transient photocurrent response.

(D) Electrochemical impedance spectra of $C_3N_4$, $Pt/C_3N_4$, $Pt_{Nv}/C_3N_4(Nv_{550})$, $Pt_{Nv}/C_3N_4(Nv_{600})$, and $Pt_{Nv}/C_3N_4(Nv_{650})$.

For photocatalysis, the dynamic behavior of photon exciton is important. Steady-state photoluminescence (PL) measurements were conducted to study the separation efficiency of photogenerated electron-hole pairs. As shown in Figure 5A, $C_3N_4$ has the strongest fluorescence intensity (PL signal) among the rage of 400–650 nm, indicating that most of the photogenerated electron are recombined with holes to generate fluorescence. After loading Pt single atom, the intensity obviously reduces, indicating that the deposition of Pt single atoms impedes the recombination of photogenerated electron-hole pairs. Moreover, further creating nitrogen vacancy onto $C_3N_4$ could reduce the PL signal. Notably, the intensity dramatically decreases for $Pt_{Nv}/C_3N_4(Nv_{600})$ and $Pt_{Nv}/C_3N_4(Nv_{650})$, insinuating that the single-atom Pt and neighboring nitrogen vacancy has a synergistic effect on the suppressing of recombination of photogenerated charge carriers.[49] This could be due to the polarization when single-atom Pt and nitrogen vacancy coexists, which can be evident in XPS. As a consequence, the lifetime of exciton is significantly extended. Time-resolved PL spectra were further conducted to analyze the decay kinetics of photogenerated electron carriers. The spectra are displayed in Figure 5B, and the fitted parameters are shown in Table S4. $Pt_{Nv}/C_3N_4(Nv)$ exhibit slow decay kinetics compared to those of single-atom $Pt/C_3N_4$ and pristine $C_3N_4$. The average exciton lifetime of $Pt_{Nv}/C_3N_4(Nv_{650})$ is 10.5 ns, which is almost twice that of $C_3N_4$ and significantly higher than that of others. These imply that the introduction of single-atom Pt and nitrogen vacancy generates impurity level, changes the dynamic features of photogenerated charge carriers, and slows down the migration and recombination rate of photogenerated electrons and holes.

Transient photocurrent response tests were conducted to investigate the migration of photogenerated charge carriers in the samples. As shown in Figure 5C, the photocurrent responses of $Pt_{Nv}/C_3N_4(Nv)$ are all much higher than those of the pristine $C_3N_4$ sample. Moreover, $Pt_{Nv}/C_3N_4(Nv_{650})$ with the most nitrogen vacancies have the highest current density response. This indicates that single-atom Pt and the nitrogen vacancies synergistically improve the separation efficiency of photogenerated charge carriers in $C_3N_4$, which is beneficial for improving the photocatalytic hydrogen production activity. The photocurrent response curve decreases continuously as time prolongs, attributed to the formation of bubbles adhering to the sample during testing, causing sample detachment, which in turn leads to a decrease in the photoelectric current response curve over time. This is more severe for $Pt_{Nv}/C_3N_4(Nv_{650})$ and $Pt_{Nv}/C_3N_4(Nv_{600})$, which have higher activity for $H_2$ generation. Also, according to the electrochemical impedance spectroscopy (EIS) plots (Figure 5D), $Pt_{Nv}/C_3N_4(Nv_{650})$ has the smallest semicircle radius, indicative of its lowest surface resistance and highest charge transfer efficiency. This is consistent with the results from the transient photocurrent response test. The corresponding Nyquist equivalent circuit diagram is also depicted, where $R_1$, $R_2$, and $C_1$ represent the charge transfer resistances of the electrolyte solution (in this case, 0.5 M $Na_2SO_4$), the working electrode, and the constant phase element (CPE), respectively. A smaller $R_2$ value corresponds to a lower charge transfer resistance and faster transfer rate. After fitting the Nyquist plot, the $R_2$ values for $C_3N_4$, $Pt/C_3N_4$, $Pt_{Nv}/C_3N_4(Nv_{550})$, $Pt_{Nv}/C_3N_4(Nv_{600})$, and $Pt_{Nv}/C_3N_4(Nv_{650})$ were measured to be 7,108, 6,803, 6,294, 6,179, and 4,951 Ω, respectively, which show an inverse trend between the pretreated temperature and the $R_2$. $Pt_{Nv}/C_3N_4(Nv_{650})$ owns the lowest $R_2$ value, suggesting that the synergistic interaction between single-atom Pt and nitrogen vacancies effectively suppresses the recombination

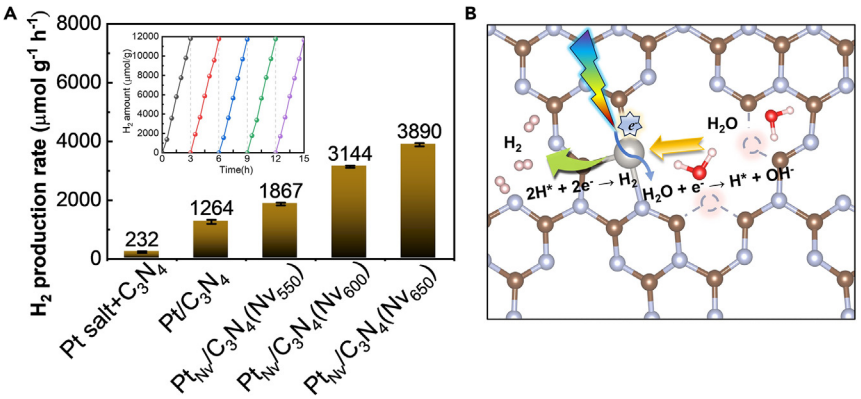


**Figure 6. Performance and mechanism of water splitting over $Pt_{Nv}/C_3N_4(Nv)$**

$H_2$ production rates of (A) $C_3N_4$, $Pt/C_3N_4$, $Pt_{Nv}/C_3N_4(Nv_{550})$, $Pt_{Nv}/C_3N_4(Nv_{600})$, and $Pt_{Nv}/C_3N_4(Nv_{650})$. Inset is the cycle stability test of $Pt_{Nv}/C_3N_4(Nv_{650})$. ($\lambda \geq$ 420 nm); (B) proposed mechanism of the photocatalytic $H_2$ evolution on $Pt_{Nv}/C_3N_4(Nv2)$.

of photogenerated charge carriers, thereby enabling highly efficient photocatalytic hydrogen evolution performance. On the basis of the aforementioned study on theoretical calculations and characterizations, the presence of single Pt dopants in $C_3N_4$ and nitrogen vacancies can both present advantage in molecular and electronic structures for the photocatalytic $H_2$ evolution from water. The coexistence of Pt dopants and nitrogen vacancies can significantly boosts these benefits, and the synergy is thus proposed.

## Photocatalytic hydrogen evolution

$H_2$ evolution from water under visible light was then employed to compare $C_3N_4$, $Pt/C_3N_4$, and $Pt_{Nv}/C_3N_4(Nv)$. To substantiate that the enhanced photocatalytic hydrogen production capability of $C_3N_4$ is not exclusively due to the incorporation of nitrogen vacancies, experiments investigating varying concentrations of nitrogen vacancies were also conducted. Pristine $C_3N_4$ exhibits an increasing trend in hydrogen-generation efficiency with increased concentration of nitrogen vacancies (Figure S13). This is reasonable as the introduction of nitrogen vacancy into the $C_3N_4$ framework could narrow the band gap and introduce a new defect level which can retard the recombination of photoelectron and hole and thus improve the photocatalytic performance. When single-atom Pt is loaded onto the $C_3N_4(Nv)$, photocatalytic hydrogen production performance is further enhanced (as depicted in Figure 6A). Similarly, Pt supported on $C_3N_4(Nv)$ pretreated at higher temperature with higher nitrogen vacancy concentrations presents better hydrogen production performance, indicating a clear synergistic promotion of nitrogen vacancies and single-atomic Pt dopants. $Pt_{Nv}/C_3N_4(Nv_{650})$ exhibits the highest photocatalytic activity with a hydrogen production rate of up to 3,890 μmol/g/h, which is 16.8 times, 4.4 times, and 3.1 times that of $C_3N_4$ (232 μmol/g/h), $C_3N_4(Nv_{650})$ (894 μmol/g/h), and $Pt/C_3N_4$ (1,264 μmol/g/h), respectively. The apparent quantum efficiency (AQE) of $Pt_{Nv}/C_3N_4(Nv_{650})$ is 5.05% at 420 nm. The significantly improved hydrogen production performance of $Pt_{Nv}/C_3N_4(Nv_{650})$ catalyst can be concluded due to the introduction of Pt single atoms and the nitrogen vacancies. Firstly, the introduction of single-atom Pt provides active sites conducive to photocatalytic hydrogen production. Secondly, the narrower band gap (2.47 eV) of $Pt_{Nv}/C_3N_4(Nv_{650})$ extends the range of light response, thereby enhancing the utilization efficiency of visible light. Thirdly, the introduction of single-atom Pt and nitrogen vacancies in $Pt_{Nv}/C_3N_4(Nv_{650})$ promotes the separation of photogenerated charge carriers and accelerates the migration rates of photogenerated electrons and holes. More importantly, the synergistic interaction between single-atom Pt and nitrogen vacancies in $Pt_{Nv}/C_3N_4(Nv_{650})$ promotes the activation of water and reduces the energy barrier for $H_2$ generation, thus boosting the photocatalytic hydrogen evolution performance. Actually, both the synergy and the electronic structure optimization by introducing nitrogen vacancies play roles in the performance enhancement. The hydrogen production performance of carbon nitride exhibits an ascending trend with the rise of nitrogen vacancy concentration, indicating that the electronic structure optimization by introducing nitrogen vacancies promotes the catalytic performance. However, this improvement does not surpass that observed when platinum (Pt) is loaded (Figure S14). For example, the catalytic performance enhancement of $C_3N_4(Nv_{650})$ compared to $C_3N_4$ is 662 μmol/g/h. The catalytic performance difference for $Pt_{Nv}/C_3N_4(Nv_{650})$ and $Pt/C_3N_4$ increases to 2,626 μmol/g/h. The significant increment reflects that a synergy should exist between the nitrogen vacancies and single Pt atoms. Geometrically, with platinum atoms neighboring nitrogen vacancies, there is an enhanced affinity for water molecule adsorption. Additionally, the lowering of the platinum d-band center decreases the adsorption capability for hydrogen atoms, thereby facilitating the evolution of hydrogen gas (Figure 6B). Compared with other reported photocatalysts listed in Table S6, $Pt_{Nv}/C_3N_4(Nv)$ exhibits superior photocatalytic hydrogen production activity. Additionally, there is no notable decrease in the hydrogen production rate for 15 h after five cycles (Figure 6A inset) over $Pt_{Nv}/C_3N_4(Nv_{650})$. The spent catalyst was collected and characterized with XRD and HRTEM (Figure S15); no obvious aggregation can be observed indicative of atomic dispersed Pt species. The catalyst is further applied in photocatalytic hydrogen production from seawater, which is among more than 95% of water resources on the Earth' surface. The results (Figure S16) demonstrate that the catalyst is also effective for photocatalytic decomposition of seawater in producing hydrogen, with an optimal hydrogen production rate of 3,796 μmol/g/h. These findings collectively highlight the excellent photocatalytic performance, stability, and versatility of the $Pt_{Nv}/C_3N_4(Nv)$ catalyst, making it a promising candidate for practical applications as the

desalination of seawater is costly. The ability to efficiently utilize seawater as a feedstock further enhances the potential application of this catalyst for sustainable and environmentally friendly energy production.

## Conclusion

In summary, we have successfully supported single-atomic Pt dopants onto nitrogen-doped carbon rich in nitrogen vacancies through a wet impregnation method. The optimized photocatalyst, $Pt_{Nv}/C_3N_4(Nv_{650})$, exhibits a hydrogen production rate of 3,890 μmol/g/h under visible light, which is approximately 16.8 times higher than that of the pristine $C_3N_4$ (232 μmol/g/h). The enhanced photocatalytic performance can be attributed to the synergistic effect between nitrogen vacancies and single-atomic Pt dopants, which promotes the separation of photogenerated carriers and increases the migration rate of photogenerated charges. This could be supported from the DFT calculation and experimental characterizations. $Pt_{Nv}/C_3N_4(Nv_{650})$ has a narrower band gap, thus exhibiting stronger responsiveness to visible light, making it easier for charges to transfer to the Pt active sites. The effective coordination between Pt and nitrogen in the system, as well as the synergistic effect between Pt and nitrogen vacancies, is beneficial for the migration of photogenerated carriers and the extension of their lifetime. Consequently, excellent catalytic stability, rapid charge transfer, and faster kinetics could be afforded through this catalytic system. This study has introduced a new understanding on the coordinated environment of catalytic active site for single atom-loaded $C_3N_4$ during the heterogeneous catalytic reactions. It provides new insights into the design of efficient catalysts and the understanding on the single-atom catalysis. Moreover, this catalyst is also effective for photocatalytic hydrogen production from seawater decomposition, with a hydrogen production rate of 3,796 μmol/g/h without obvious attenuations, revealing its potential applicability.

## Limitations of the study

Our research, by combining theoretical calculations with experimental validations, has jointly confirmed that the synergistic effect between single-atom platinum and nitrogen vacancies facilitates the modulation of the band structure of graphitic carbon nitride, enhancing its responsiveness to light and facilitating the separation and migration of photogenerated electrons and holes. This significantly boosts the performance of carbon nitride in photocatalytic water splitting. Nonetheless, overall water splitting has more practical meaning in real world. In future, we will aim to explore its application in overall water splitting, thereby advancing toward a green and sustainable development.

## STAR★METHODS

Detailed methods are provided in the online version of this paper and include the following:

- KEY RESOURCES TABLE
- RESOURCE AVAILABILITY
  - Lead contact
  - Materials availability
  - Data and code availability
- EXPERIMENTAL MODEL AND STUDY PARTICIPANT DETAILS
- METHOD DETAILS
  - Catalyst preparation method
  - Characterization methods
  - Photocatalytic water splitting test
  - Photoelectrochemical test
  - Photocurrent Characterization (i-t)
  - Electrochemical Impedance Spectroscopy (EIS)
- QUANTIFICATION AND STATISTICAL ANALYSIS

## SUPPLEMENTAL INFORMATION

Supplemental information can be found online at https://doi.org/10.1016/j.isci.2024.110420.

## ACKNOWLEDGMENTS

This work is supported by the National Natural Science Foundation of China (NSFC) (22372135), Natural Science Foundation of Xiamen, China (3502Z202373001), the Fundamental Research Funds for the Central Universities (20720230007), National Key Research and Development Program of China (2022YFB4101000), and NSFC (92361303).

## AUTHOR CONTRIBUTIONS

A.-P.Y. designed and conducted the experiments and wrote the experimental section of the paper; Y.-J.Q. built the models, conducted theoretical analysis, and wrote the theoretical section of the paper; X.-E.W., X.-T.L., X.-D.C., and X.S. conducted the characterizations including XRD, UV-vis, etc. G.-H.W. and X.-K.W. conducted the STEM-HAADF; A.-P.Y. and Y.-J.Q. equally contributed to this work and should be considered as co-first authors. S.-L.D. participated in the discussion. J.-W.Z. wrote the manuscript. J.-W.Z. and S.-Y.X. conceived the overall

project. All authors approved the final version of the manuscript. All authors had full access to the data and had the final responsibility for the decision to submit for publication.

## DECLARATION OF INTERESTS

The authors declare no competing interests.

Received: March 30, 2024
Revised: May 9, 2024
Accepted: June 27, 2024
Published: June 29, 2024

## REFERENCES

1. Gao, Y., Song, T., Guo, X., Zhang, Y., and Yang, Y. (2023). Electronic interaction and oxygen vacancy engineering of g-$C_3N_4$/α-$Bi_2O_3$ Z-scheme heterojunction for enhanced photocatalytic aerobic oxidative homo-/hetero-coupling of amines to imines in aqueous phase. Green Carbon *1*, 105–117. https://doi.org/10.1016/j.greenca.2023.09.004.
2. Sun, S., and Liang, S. (2017). Recent advances in functional mesoporous graphitic carbon nitride (mpg-$C_3N_4$) polymers. Nanoscale *9*, 10544–10578. https://doi.org/10.1039/C7NR03656F.
3. Yang, H., Sun, S., Lyu, J., Yang, Q., and Cui, J. (2024). Mechanism insight into triple S-Scheme intermolecular carbon nitride homojunction with robust built-in electric field for highly enhanced photocatalytic hydrogen evolution. Chem. Eng. J. *481*, 148297. https://doi.org/10.1016/j.cej.2023.148297.
4. Zhao, D., Chen, J., Dong, C.-L., Zhou, W., Huang, Y.-C., Mao, S.S., Guo, L., and Shen, S. (2017). Interlayer interaction in ultrathin nanosheets of graphitic carbon nitride for efficient photocatalytic hydrogen evolution. J. Catal. *352*, 491–497. https://doi.org/10.1016/j.jcat.2017.06.020.
5. Zhao, D., Dong, C.-L., Wang, B., Chen, C., Huang, Y.-C., Diao, Z., Li, S., Guo, L., and Shen, S. (2019). Synergy of dopants and defects in graphitic carbon nitride with exceptionally modulated band structures for efficient photocatalytic oxygen evolution. Adv. Mater. *31*, 1903545. https://doi.org/10.1002/adma.201903545.
6. Zhang, J., Zhu, Q., Ma, Y., Wang, L., Nasir, M., and Zhang, J. (2021). Photo-generated charges escape from $P^+$ center through the chemical bridges between P-doped g-$C_3N_4$ and $Ru_xP$ nanoparticles to enhance the photocatalytic hydrogen evolution. Catal. Today *380*, 223–229. https://doi.org/10.1016/j.cattod.2020.12.037.
7. Huang, Z., Song, J., Pan, L., Wang, Z., Zhang, X.-Q., Zou, J.-J., Mi, W., Zhang, X., and Wang, L. (2015). Carbon nitride with simultaneous porous network and O-doping for efficient solar-energy-driven hydrogen evolution. Nano Energy *12*, 646–656. https://doi.org/10.1016/j.nanoen.2015.01.043.
8. Yang, C., Tan, Q., Li, Q., Zhou, J., Fan, J., Li, B., Sun, J., and Lv, K. (2020). 2D/2D $Ti_3C_2$ MXene/g-$C_3N_4$ nanosheets heterojunction for high efficient $CO_2$ reduction photocatalyst: Dual effects of urea. Appl. Catal. B Environ. *268*, 118738. https://doi.org/10.1016/j.apcatb.2020.118738.
9. Chu, X., Qu, Y., Zada, A., Bai, L., Li, Z., Yang, F., Zhao, L., Zhang, G., Sun, X., Yang, Z.-D., and Jing, L. (2020). Ultrathin Phosphate-Modulated Co Phthalocyanine/g-$C_3N_4$ Heterojunction Photocatalysts with Single Co–$N_4$ (II) Sites for Efficient $O_2$ Activation. Adv. Sci. *7*, 2001543. https://doi.org/10.1002/advs.202001543.
10. Sun, S., Li, J., Song, P., Cui, J., Yang, Q., Zheng, X., Yang, Z., and Liang, S. (2020). Facile constructing of isotype g-$C_3N_4$(bulk)/g-$C_3N_4$ (nanosheet) heterojunctions through thermal polymerization of single-source glucose-modified melamine: An efficient charge separation system for photocatalytic hydrogen production. Appl. Surf. Sci. *500*, 143985. https://doi.org/10.1016/j.apsusc.2019.143985.
11. Zhai, H., Liu, H., Zhang, Y., Tong, J., Liu, X., Du, W., Liao, H., Tan, P., and Pan, J. (2024). Flexible construction of heteroatom-free g-$C_3N_4$/g-$C_3N_4$ homojunction with switching charge dynamics toward efficient photo-piezocatalytic performance. Appl. Catal. B Environ. *349*, 123909. https://doi.org/10.1016/j.apcatb.2024.123909.
12. Yang, H., Sun, S., Duan, R., Yang, B., Yang, M., Qi, X., Cai, C., Yun, D., Yang, Q., and Cui, J. (2023). Mechanism insight into enhanced photocatalytic hydrogen production by nitrogen vacancy-induced creating built-in electric field in porous graphitic carbon nitride nanosheets. Appl. Surf. Sci. *631*, 157544. https://doi.org/10.1016/j.apsusc.2023.157544.
13. Ren, J., Chi, H.Y., Tan, L., Peng, Y.K., Li, G.C., Li, M.M.J., Zhao, Y.F., and Duan, X. (2023). Semi-quantitative determination of active sites in heterogeneous catalysts for photo/electrocatalysis. J. Mater. Chem. A *11*, 2528–2543. https://doi.org/10.1039/d2ta09033c.
14. Li, W., Dang, Y., Li, J., Ma, T., Liao, G., Gao, F., Duan, W., Li, J., Wang, X., and Wang, C. (2023). Nanoconfinement dynamics and crystal plane exposure: Synergistic promotion of simulated solar-driven $H_2O$-to-$H_2$ conversion on host (CdS)-guest (Ti single-atom) nano-photocatalyst. Chem. Eng. J. *472*, 144793. https://doi.org/10.1016/j.cej.2023.144793.
15. Ma, T., Li, W., Li, J., Duan, W., Gao, F., Liao, G., Li, J., and Wang, C. (2024). Multisite Cocatalysis: Single atomic $Pt^{2+}$/$Pt^0$ active sites synergistically improve the simulated sunlight driven $H_2O$-to-$H_2$ conversion performance of $Sb_2S_3$ nanorods. J. Colloid Interface Sci. *658*, 476–486. https://doi.org/10.1016/j.jcis.2023.12.087.
16. Gao, G., Jiao, Y., Waclawik, E.R., and Du, A. (2016). Single atom (Pd/Pt) supported on graphitic carbon nitride as an efficient photocatalyst for visible-light reduction of carbon dioxide. J. Am. Chem. Soc. *138*, 6292–6297. https://doi.org/10.1021/jacs.6b02692.
17. Yin, H., Li, S.-L., Gan, L.-Y., and Wang, P. (2019). Pt-embedded in monolayer g-$C_3N_4$ as a promising single-atom electrocatalyst for ammonia synthesis. J. Mater. Chem. A *7*, 11908–11914. https://doi.org/10.1039/C9TA01624D.
18. Le Bahers, T., Rérat, M., and Sautet, P. (2014). Semiconductors used in photovoltaic and photocatalytic devices: assessing fundamental properties from DFT. J. Phys. Chem. C *118*, 5997–6008. https://doi.org/10.1021/jp409724c.
19. Clarke, T.M., and Durrant, J.R. (2010). Charge photogeneration in organic solar cells. Chem. Rev. *110*, 6736–6767. https://doi.org/10.1021/cr900271s.
20. Yuan, J., Tang, Y., Yi, X., Liu, C., Li, C., Zeng, Y., and Luo, S. (2019). Crystallization, cyanamide defect and ion induction of carbon nitride: Exciton polarization dissociation, charge transfer and surface electron density for enhanced hydrogen evolution. Appl. Catal. B Environ. *251*, 206–212. https://doi.org/10.1016/j.apcatb.2019.03.069.
21. Yang, X.-F., Wang, A., Qiao, B., Li, J., Liu, J., and Zhang, T. (2013). Single-atom catalysts: A new frontier in heterogeneous catalysis. Acc. Chem. Res. *46*, 1740–1748. https://doi.org/10.1021/ar300361m.
22. Hang Li, Y., Xing, J., Jia Chen, Z., Li, Z., Tian, F., Rong Zheng, L., Feng Wang, H., Hu, P., Jun Zhao, H., and Gui Yang, H. (2013). Unidirectional suppression of hydrogen oxidation on oxidized platinum clusters. Nat. Commun. *4*, 2500. https://doi.org/10.1038/ncomms3500.
23. Li, Y.H., Peng, C., Yang, S., Wang, H.F., and Yang, H.G. (2015). Critical roles of co-catalysts for molecular hydrogen formation in photocatalysis. J. Catal. *330*, 120–128. https://doi.org/10.1016/j.jcat.2015.07.009.
24. Huang, L., Sun, J.-Y., Cao, S.-H., Zhan, M., Ni, Z.-R., Sun, H.-J., Chen, Z., Zhou, Z.-Y., Sorte, E.G., Tong, Y.J., and Sun, S.-G. (2016). Combined EC-NMR and *in situ* FTIR spectroscopic studies of glycerol electrooxidation on Pt/C, PtRu/C, and PtRh/C. ACS Catal. *6*, 7686–7695. https://doi.org/10.1021/acscatal.6b02097.
25. Han, X., Liu, Q., Qian, A., Ye, L., Pu, X., Liu, J., Jia, X., Wang, R., Ju, F., Sun, H., et al. (2023). Transition-metal single atom anchored on $MoS_2$ for enhancing photocatalytic hydrogen production of g-$C_3N_4$ photocatalysts. ACS

Appl. Mater. Interfaces *15*, 26670–26681. https://doi.org/10.1021/acsami.3c02895.

26. Zhai, H., Tan, P., Jiang, M., Zhang, M., Ren, R., Sa, R., and Pan, J. (2023). Electronic regulation of Pt single-atom catalysts via local coordination state adjustment for enhanced photocatalytic performance. ACS Catal. *13*, 8063–8072. https://doi.org/10.1021/acscatal.3c01141.
27. Zhang, W., Peng, Q., Shi, L., Yao, Q., Wang, X., Yu, A., Chen, Z., and Fu, Y. (2019). Merging single-atom-dispersed iron and graphitic carbon nitride to a joint electronic system for high-efficiency photocatalytic hydrogen evolution. Small *15*, e1905166. https://doi.org/10.1002/smll.201905166.
28. Wang, G., Zhang, T., Yu, W., Si, R., Liu, Y., and Zhao, Z. (2020). Modulating location of single copper atoms in polymeric carbon nitride for enhanced photo-redox catalysis. ACS Catal. *10*, 5715–5722. https://doi.org/10.1021/acscatal.0c01099.
29. Liu, Y., Sun, J., Huang, H., Bai, L., Zhao, X., Qu, B., Xiong, L., Bai, F., Tang, J., and Jing, L. (2023). Improving $CO_2$ photoconversion with ionic liquid and Co single atoms. Nat. Commun. *14*, 1457. https://doi.org/10.1038/s41467-023-36980-5.
30. Wang, Y., Qu, Y., Qu, B., Bai, L., Liu, Y., Yang, Z.-D., Zhang, W., Jing, L., and Fu, H. (2021). Construction of six-oxygen-coordinated single Ni sites on g-$C_3N_4$ with boron-oxo species for photocatalytic water-activation-induced $CO_2$ reduction. Adv. Mater. *33*, 2105482. https://doi.org/10.1002/adma.202105482.
31. Liu, J., Jiao, M., Lu, L., Bark Holtz, H.M., Li, Y., Wang, Y., Jiang, L., Wu, Z., Liu, D.-J., Zhuang, L., et al. (2017). High performance platinum single atom electrocatalyst for oxygen reduction reaction. Nat. Commun. *8*, 15938. https://doi.org/10.1038/ncomms15938.
32. Xue, Y., Lei, Y., Liu, X., Li, Y., Deng, W., Wang, F., and Min, S. (2018). Highly active dye-sensitized photocatalytic $H_2$ evolution catalyzed by a single-atom Pt cocatalyst anchored onto g-$C_3N_4$ nanosheets under long-wavelength visible light irradiation. New J. Chem. *42*, 14083–14086. https://doi.org/10.1039/C8NJ02933D.
33. Zhou, P., Lv, F., Li, N., Zhang, Y., Mu, Z., Tang, Y., Lai, J., Chao, Y., Luo, M., Lin, F., et al. (2019). Strengthening reactive metal-support interaction to stabilize high-density Pt single atoms on electron-deficient g-$C_3N_4$ for boosting photocatalytic $H_2$ production. Nano Energy *56*, 127–137. https://doi.org/10.1016/j.nanoen.2018.11.033.
34. Cao, S., Li, H., Tong, T., Chen, H.-C., Yu, A., Yu, J., and Chen, H.M. (2018). Single-atom engineering of directional charge transfer channels and active sites for photocatalytic hydrogen evolution. Adv. Funct. Mater. *28*, 1802169. https://doi.org/10.1002/adfm.201802169.
35. Zeng, Z., Su, Y., Quan, X., Choi, W., Zhang, G., Liu, N., Kim, B., Chen, S., Yu, H., and Zhang, S. (2020). Single-atom platinum confined by the interlayer nano-space of carbon nitride for efficient photocatalytic hydrogen evolution. Nano Energy *69*, 104409. https://doi.org/10.1016/j.nanoen.2019.104409.
36. Xiao, X., Gao, Y., Zhang, L., Zhang, J., Zhang, Q., Li, Q., Bao, H., Zhou, J., Miao, S., Chen, N., et al. (2020). A promoted charge separation/transfer system from Cu single atoms and $C_3N_4$ layers for efficient photocatalysis. Adv. Mater. *32*, 2003082. https://doi.org/10.1002/adma.202003082.
37. Dong, G., Zhao, K., and Zhang, L. (2012). Carbon self-doping induced high electronic conductivity and photo-reactivity of g-$C_3N_4$. Chem. Commun. *48*, 6178–6180. https://doi.org/10.1039/C2CC32181E.
38. Wu, M.-Y., Da, P.-F., Zhang, T., Mao, J., Liu, H., and Ling, T. (2018). Designing hybrid $NiP_2$/NiO nanorod arrays for efficient alkaline hydrogen evolution. ACS Appl. Mater. Interfaces *10*, 17896–17902. https://doi.org/10.1021/acsami.8b02691.
39. Zhao, E., Li, M., Xu, B., Wang, X.L., Jing, Y., Ma, D., Mitchell, S., Pérez-Ramírez, J., and Chen, Z. (2022). Transfer hydrogenation with a carbon-nitride-supported palladium single-atom photocatalyst and water as a proton source. Angew. Chem. Int. Ed. *61*, e202207410. https://doi.org/10.1002/anie.202207410.
40. Duan, Y., Wang, Y., Gan, L., Meng, J., Feng, Y., Wang, K., Zhou, K., Wang, C., Han, X., and Zhou, X. (2021). Amorphous carbon nitride with three coordinate nitrogen ($N_3C$) vacancies for exceptional $NO_x$ abatement in visible light. Adv. Energy Mater. *11*, 2004001. https://doi.org/10.1002/aenm.202004001.
41. Shi, L., Yang, L., Zhou, W., Liu, Y., Yin, L., Hai, X., Song, H., and Ye, J. (2018). Photo-assisted construction of holey defective g-$C_3N_4$ photocatalysts for efficient visible-light-driven $H_2O_2$ production. Small *14*, 1703142. https://doi.org/10.1002/smll.201703142.
42. Cheng, J., Hu, Z., Lv, K., Wu, X., Li, Q., Li, Y., Li, X., and Sun, J. (2018). Drastic promoting the visible photo-reactivity of layered carbon nitride by polymerization of dicyandiamide at high pressure. Appl. Catal. B Environ. *232*, 330–339. https://doi.org/10.1016/j.apcatb.2018.03.066.
43. Xue, Y., Ji, Y., Wang, X., Wang, H., Chen, X., Zhang, X., and Tian, J. (2023). Hetero-structuring noble-metal-free 1T′ phase $MoS_2$ with g-$C_3N_4$ hollow nanocages to improve the photocatalytic $H_2$ evolution activity. Green Energy Environ. *8*, 864–873. https://doi.org/10.1016/j.gee.2021.11.002.
44. Zhang, R., Zhang, X., Liu, S., Tong, J., Kong, F., Sun, N., Han, X., and Zhang, Y. (2021). Enhanced photocatalytic activity and optical response mechanism of porous graphitic carbon nitride (g-$C_3N_4$) nanosheets. Mater. Res. Bull. *140*, 111263. https://doi.org/10.1016/j.materresbull.2021.111263.
45. Cheng, N., Stambula, S., Wang, D., Banis, M.N., Liu, J., Riese, A., Xiao, B., Li, R., Sham, T.-K., Liu, L.-M., et al. (2016). Platinum single-atom and cluster catalysis of the hydrogen evolution reaction. Nat. Commun. *7*, 13638. https://doi.org/10.1038/ncomms13638.
46. Li, X., Bi, W., Zhang, L., Tao, S., Chu, W., Zhang, Q., Luo, Y., Wu, C., and Xie, Y. (2016). Single-atom Pt as co-catalyst for enhanced photocatalytic $H_2$ evolution. Adv. Mater. *28*, 2427–2431. https://doi.org/10.1002/adma.201505281.
47. Xue, Y., Wang, X., Liang, Z., Zhang, X., and Tian, J. (2022). The fabrication of graphitic carbon nitride hollow nanocages with semi-metal 1T′ phase molybdenum disulfide as co-catalysts for excellent photocatalytic nitrogen fixation. J. Colloid Interface Sci. *608*, 1229–1237. https://doi.org/10.1016/j.jcis.2021.10.153.
48. Tu, W., Xu, Y., Wang, J., Zhang, B., Zhou, T., Yin, S., Wu, S., Li, C., Huang, Y., Zhou, Y., et al. (2017). Investigating the role of tunable nitrogen vacancies in graphitic carbon nitride nanosheets for efficient visible-light-driven $H_2$ evolution and $CO_2$ reduction. ACS Sustain. Chem. Eng. *5*, 7260–7268. https://doi.org/10.1021/acssuschemeng.7b01477.
49. Wang, Y., Xia, Q., Bai, X., Ge, Z., Yang, Q., Yin, C., Kang, S., Dong, M., and Li, X. (2018). Carbothermal activation synthesis of 3D porous g-$C_3N_4$/carbon nanosheets composite with superior performance for $CO_2$ photoreduction. Appl. Catal. B Environ. *239*, 196–203. https://doi.org/10.1016/j.apcatb.2018.08.018.

## STAR★METHODS

### KEY RESOURCES TABLE

| REAGENT or RESOURCE | SOURCE | IDENTIFIER |
|---|---|---|
| Chemicals, peptides, and recombinant proteins | | |
| Urea | Aladdin | 57-13-6 |
| $H_2PtCl_6$ | Sinopharm Chemical Reagent Co.,Ltd | 16941-12-1 |
| $C_6H_{15}NO_3$ | Sinopharm Chemical Reagent Co.,Ltd | 102-71-6 |
| $N_2$ (99.999%) | MESSER | 7727-37-9 |
| Ar (99.999%) | MESSER | 7440-37-1 |

### RESOURCE AVAILABILITY

#### Lead contact

Further information and request for resources should be directed to and will be fulfilled by the lead contact, Jian-Wei Zheng (jwzheng@xmu.edu.cn).

#### Materials availability

This study did not generate new unique reagents.

#### Data and code availability

- Pseudonymized data reported in this paper will be shared by the lead contact upon request.
- This paper does not report original code.
- Any additional information required to reanalyze the data reported in this paper is available from the lead contact upon request.

### EXPERIMENTAL MODEL AND STUDY PARTICIPANT DETAILS

The DFT simulated calculation was carried out using the Vienna ab initio simulation package (VASP). A two dimensional (2D) melon sheet was constructed, with a large vacuum space of 15 Å to separate two neighboring 2D melon sheets, and the (2×2) supercell was used here. A cubic cell was adopted for the carbon nitrides materials with experimental lattice constants of a = 14.25 Å and b = 14.25 Å. The generalized gradient approximation (GGA) with Perdew-Burke-Ernzerhof (PBE) functional was employed for the DFT exchange correlation energy, and a 450 eV cutoff was assigned to the plane-wave basis set. The k -point meshes in the Brillouin zone integration were sampled by 2×2×1 for the surface. The electronic energy is considered self−consistent when the energy change is smaller than $10^{-5}$ eV, and all structures were relaxed until forces on atoms less than 0.01 eV/Å. Since the van der Waals (vdW) interaction is expected to be important in these layered structures, in this work, we adopt the DFT-D3 correction.

To overcome the disadvantages of standard DFT-PBE calculations in computing an accurate band gap, we employed the Heyd–Scuseria–Ernzerhof (HSE06) hybrid functional with mixing parameter of 0.25.

The adsorption energy ($E_{ads}$) of Pt atoms at the surface of various g-$C_3N_4$ was used to evaluate the stability of coordination structure, which was calculated by the following equation:

$$\Delta E_{ads} = E_{slab\ +\ Pt} - E_{slab} - E_{Pt} \quad \text{(Equation 4)}$$

Where $E_{slab\ +\ Pt}$ is the total energy for the adsorption Pt, $E_{slab}$ is the energy of pure surface, and $E_{Pt}$ is the energy of Pt in gas phase.

The adsorption energy of reaction intermediates can be computed using the following equations:

$$\Delta G = \Delta E + \Delta E_{ZPE} - T\Delta S \quad \text{(Equation 5)}$$

$$\Delta E = E_{slab\ +\ ads*} - E_{slab} - E_{ads} \quad \text{(Equation 6)}$$

Where $\Delta E_{ZPE}$ is the zero-point energy change and $\Delta S$ is the entropy change. $T$ is the temperature (298.15 K).

## METHOD DETAILS

### Catalyst preparation method

1) Synthesis of $C_3N_4$: 8 g of urea was weighted in a covered crucible. The crucible was then transferred into a muffle furnace and heated to 550°C at a heating rate of 5°C /min for 4 hours. After cooling to room temperature, the pale yellow solid of $C_3N_4$ was collected.
2) Synthesis of $C_3N_4$(Nv): 200 mg of $C_3N_4$ was heated to 550°C、600°C or 650°C at a heating rate of 5°C/min in a nitrogen atmosphere for 180 minutes. After cooling to room temperature, $C_3N_4(Nv_{550})$、$C_3N_4(Nv_{600})$ and $C_3N_4(Nv_{650})$ were obtained.
3) Synthesis of $Pt/C_3N_4$ or $Pt_{Nv}/C_3N_4$(Nv): 50 mg of $C_3N_4$ or $C_3N_4$(Nv) was placed in a 50 mL round-bottom flask. 15 mL of deionized water was added and the obtained solution is sonicated for 10 minutes. Subsequently, 0.5 mL of chloroplatinic acid (2 mg/mL) was added into the solution under sonication for 10 minutes and aged at 70°C in an oil bath for 6 hours and then cooled down to room temperature. Afterwards, the solution was centrifugated and washed with water and ethanol prior to being dried at 60°C. Then the solid was heated at 125°C with a heating rate of 2°C/min in an argon atmosphere for 1 h. After cooling to room temperature, the target products of $Pt/C_3N_4$ or $Pt_{Nv}/C_3N_4$(Nv) was obtained.

### Characterization methods

Scanning electron microscopy (SEM) was characterized by Sigma electron microscope (ZEISS SIGMA, Germany). The transmission electron microscope (TEM) image was obtained on a Tecnai F30 electron microscope (FEI, Netherlands) with a 300 kV accelerating voltage. X-ray diffraction (XRD) were measured by an X-ray diffractometer (Rigaku, Japan) with Cu Kα radiation (λ = 1.5418 Å) at a scan rate of 10°/min. Fourier transformed infrared (FT-IR) test were conducted on a Nicolet N6700 FTIR spectrometer. X-ray photoelectron spectroscopy (XPS) was performed on a Thermo Scientific ESCALAB 250 spectrometer with Al Kα radiation as the excitation source. $N_2$ adsorption-desorption isotherms at 77 K were measured by $N_2$ adsorption apparatus (Tristar II 3020, USA). UV-visible spectrophotometer (Varian Cary 5000) was utilized to record UV-vis diffuse reflectance spectra. Photoluminescence (PL) spectra was obtained by a fluorescence spectrophotometer (F-7000, Hitachi, Japan) with the excitation wavelength of 300 nm. Transition photocurrent response spectra (PC) and electrochemical impedance spectroscopy (EIS) were recorded by electrochemical workstation (CHI660E). During testing, the 300W xenon lamp with a filter ($\lambda \geq 420$ nm) was used as simulated visible light. While the platinum sheet was used as the counter electrode, Ag/AgCl (saturated KCl solution) as the reference electrode, and 0.5 M sodium sulfate solution as the electrolyte.

Details of characterizing the solid phase with X-ray absorption fine structure (XAFS) analyses: Pt $L_3$-edge analysis was performed with Si(111) crystal monochromators at the XAFCA beamlines at the Singapore Synchrotron Light Source, SSLS. Before the analysis at the beamline, samples were pressed into thin sheets with 1 cm in diameter and sealed using Kapton tape film. The XAFS spectra were recorded at room temperature using a 4-channel Silicon Drift Detector (SDD) Bruker 5040. Pt extended X-ray absorption fine structure (EXAFS) spectra were recorded in transmission mode at 700 MeV and 200 mA. Negligible changes in the line-shape and peak position of Pt $L_3$-edge XANES spectra were observed between two scans taken for a specific sample. The XAFS spectra of Pt foil standard sample were recorded in transmission mode. The spectra were processed and analyzed by the software codes Athena and Artemis.

In order to obtain specific structural parameters surrounding platinum atoms in the pre-treated samples, quantitative curve fittings were performed on the $k^3$-weighted $\chi(k)$ data transformed into real (R) space, utilizing the ARTEMIS module within the IFEFFIT3 software package. The effective backscattering amplitudes F(k) and phase shifts $\Phi(k)$ for all fitting paths were calculated using the ab initio code FEFF8.0. During the fitting analysis, the amplitude reduction factor S02 was fixed to the optimal fitting value of 0.70, which was determined through fitting the reference samples of bulk metal platinum, bulk $PtN_2$, and bulk $PtCl_4$.

### Photocatalytic water splitting test

The photocatalytic hydrogen evaluation system was purchased from Beijing Zhong Jiao Jin Yuan Science & Technology Co., Ltd. The system consists of a photocatalytic reaction device, a gas collection device, and a gas detection device. The photocatalytic reaction device is a 200 mL quartz glass container with sealing rings and a translucent quartz cover. The light source used is a xenon lamp with model CEL-HXF300, power of 300 W, and a wavelength range of 350-780 nm. After passing through a filter with a wavelength of 420 nm, the wavelength range becomes 420-780 nm. The gas collection device consists of glass pipes and an automatic sampler, set to automatically sample once every 30 minutes. The gas detection device is a gas chromatograph with model GC7920-TF2Z, using high-purity argon gas with a purity of 99.999% as the carrier gas.

The testing method is as follows: weigh 25 mg of the catalyst into a 200 mL glass container, add 90 mL of deionized water and 10 mL of triethanolamine as a sacrificial agent, and sonicate for 5 minutes to ensure thorough dispersion of the catalyst. Place the quartz glass container on a magnetic stirrer and set the rotation speed to 800 r/min so that the catalyst remains suspended during the reaction. Before turning on the light source, use a vacuum pump to remove air from the system until no bubbles appear in the solution inside the quartz glass container. Use a circulating cooling pump to set the water temperature to 6°C, ensuring constant temperature for the reaction system under prolonged illumination. Maintain a constant distance of 10 cm between the light source and the liquid surface.

The apparent quantum efficiency (AQE) measurements were conducted under the illumination of a Xe light with an irradiation density of 9.1x1000 mW/cm$^2$ through a 420 nm allowed optical filter. The area is 23.75 cm$^2$. The AQE of photocatalytic $H_2$ production was calculated using the equation:

$$AQE = 2 \times n(H_2)/n(photons) \times 100\% \quad \text{(Equation 7)}$$

In this equation, n($H_2$) represents the number of produced hydrogen molecules, and n(photons) denotes the number of incident photons. The factor of 2 in the equation accounts for the fact that each hydrogen molecule ($H_2$) is formed from two hydrogen atoms, each requiring one electron, hence two photons are needed for the overall water splitting process. The percentage calculation provides the AQE as a fraction of the maximum possible efficiency.

### Photoelectrochemical test

Electrochemical tests were conducted utilizing the Shanghai Chenhua Workstation model CHI660e. The protocol for electrode fabrication is outlined as follows: Precisely measure 4 mg of catalyst and disperse it into a mixture composed of 375 μL of ethanol, 125 μL of deionized water, and 50 μL of naphthol. The blend was subsequently subjected to ultrasonic cavitation for half an hour to guarantee homogenous dispersion of catalyst particles within the solution. Thereafter, deploy a pipette to carefully deposit the finely dispersed catalyst suspension onto the conductive face of a conductive glass substrate. Upon completion of deposition, position the slide bearing the catalyst specimen beneath an infrared heat lamp for drying purposes. This experimental setup incorporated a clear, tripartite quartz glass electrolytic chamber to establish a three-electrode configuration, employing a silver/silver chloride combination as the reference electrode, platinum (Pt) as the counter electrode, and the working electrode constituted by the conductive glass covered with the test catalyst. Electrochemical performance assessments were carried out in a 0.5 molar sodium sulfate solution functioning as the electrolyte.

### Photocurrent Characterization (i-t)

Commence by positioning the catalyst-coated conductive glass beneath a xenon illumination source. Initiate the process in darkness, allowing 100 seconds for stabilization of the dark current to negate background interferences. Thereupon, alternate the illumination cycle, activating the light source for 20-second intervals every 20 seconds, interspersed with equal periods of darkness. This sequence documents fluctuations in photocurrent over the course of 320 seconds.

### Electrochemical Impedance Spectroscopy (EIS)

The EIS measurement were performed on a CHI660e electrochemical workstation in a standard three-electrode system with a Pt wire as a counter electrode, a saturated Ag/AgCl as a reference electrode and ITO as working electrode. Initial Voltage (V): Open Circuit Potential; Upper Frequency Limit (Hz): 100,000; Lower Frequency Limit (Hz): 0.1; Perturbation Amplitude (V): 0.005; Relaxation Period (seconds): 2.

## QUANTIFICATION AND STATISTICAL ANALYSIS

■■■.